Revision 5

High-pressure Phase Transition of Olivine-type Mg_2GeO_4 to a Metastable Forsterite-III type Structure and their Equation of States.

R. Valli Divya[1], Gulshan Kumar[1], R. E. Cohen[2], Sally J. Tracy[2], Yue Meng[3], Stella Chariton[4], Vitali B. Prakapenka[4], and Rajkrishna Dutta[1, *]

[1]Department of Earth Sciences, IIT Gandhinagar, Gujarat 382355, India.
[2]Earth and Planets Laboratory, Carnegie Institution for Science, Washington DC 20015, USA.
[3]HPCAT, Advanced Photon Source, Argonne National Laboratory, Argonne, IL 60439, USA.
[4]Center for Advanced Radiation Sources, University of Chicago, Chicago, IL 60637, USA.

Abstract

Germanates are often used as structural analogs of planetary silicates. We have explored the high-pressure phase relations in Mg_2GeO_4 using diamond anvil cell experiments combined with synchrotron X-ray diffraction and computations based on density functional theory. Upon room temperature compression, forsterite-type Mg_2GeO_4 remains stable up to 30 GPa. At higher pressures, a phase transition to a forsterite-III type ($Cmc2_1$) structure was observed, which remained stable to the peak pressure of 105 GPa. Using a 3rd order Birch Murnaghan fit to the experimental data, we obtained $V_0 = 305.1\ (3)$ Å^3, $K_0 = 124.6\ (14)$ GPa and $K'_0 = 3.86$ (fixed) for forsterite- and $V_0 = 263.5\ (15)$ Å^3, $K_0 = 175\ (7)$ GPa and $K'_0 = 4.2$ (fixed) for the forsterite-III type phase. The forsterite-III type structure was found to be metastable when compared to the stable assemblage of perovskite/post-perovskite + MgO, as observed during laser-heating experiments. Understanding the phase relations and physical properties of metastable phases is crucial for studying the mineralogy of impact sites, understanding metastable wedges in subducting slabs and interpreting the results of shock compression experiments.

1. Introduction

$(Mg,Fe)_2SiO_4$ olivine is the most abundant mineral in the Earth's upper mantle. The major seismic discontinuities (410, 520 and 660 km) in the upper mantle and transition zone can be attributed to pressure induced phase transitions in Mg-rich olivine to β-olivine (wadsleyite), γ-

olivine (ringwoodite) and (Mg, Fe)SiO$_3$ perovskite (bridgmanite, Pv) + (Mg, Fe)O magnesiowüstite (Ringwood 1991). The D" layer, located in the lowermost ~250 km of the mantle is characterized by a transition from bridgmanite to post-perovskite (pPv; 125 GPa and 2500 K; Murakami et al. 2004; Oganov and Ono 2004; Tsuchiya et al. 2004). Post-perovskite (Mg, Fe)SiO$_3$ is expected to be the highest-pressure silicate phase in the Earth. However, in the case of terrestrial super-Earth planets, where the pressure-temperature conditions at the core-mantle boundary can be substantially higher (e.g., > 1600 GPa and ~6500 K for a planet with a mass equivalent to that of 10 Earths; van den Berg et al. 2019), additional transitions are possible. At ~500 GPa, pPv + MgO is expected to recombine into a tetragonal $I\bar{4}2d$ or cubic $I\bar{4}3d$ Mg$_2$SiO$_4$ phase (Umemoto et al., 2017; Dutta et al., 2023), followed by a dissociation into the binary oxides at ~3000 GPa. However, all the post-pPv transitions have only been computationally predicted and not observed experimentally because of the extreme pressure-temperature conditions, which are beyond the limits of conventional experimental techniques. As an alternative, silicate analogs like germanates (Ringwood & Seabrook, 1963; Umemoto & Wentzcovitch, 2019; Dutta et al., 2018; Dutta et al., 2022) and fluorides (Grocholski et al., 2010; Dutta et al., 2019) can be used in high-pressure experiments as they undergo similar phase transitions, but at significantly lower pressures, e.g. the Pv-pPv phase transition, which occurs at 125 GPa in MgSiO$_3$ is observed at 65 GPa in the germanate (Hirose et al. 2005). Additionally, the $I\bar{4}2d$/ $I\bar{4}3d$ phase in Mg$_2$GeO$_4$ has been reported at pressures > 170 GPa from experiments (Dutta et al., 2022) and computational studies (Umemoto and Wentzcovitch 2019, 2021) in comparison to the theoretical prediction of 500 GPa in the silicate (Umemoto et al. 2017).

There is considerable interest in understanding the 300 K compression behavior of both the silicate and germanate olivine as well. Knowledge of the metastable transitions in olivine can

help in understanding mineral phases formed at impact sites (Van de Moortèle et al. 2007). It is potentially useful in inferring phase transitions in laboratory shock experiments, where the short time scale may prevent formation of stable assemblages (Kim et al. 2021). In Mg_2SiO_4, existing studies have reported pressure induced amorphization (Guyot and Reynard 1992; Andrault et al. 1995), change in compression mechanism (Rouquette et al. 2008) or a transition to forsterite-II and forsterite-III (Finkelstein et al., 2014; referred to as Fo-II and Fo-III after this) structures. In Mg_2GeO_4, the stable phase at ambient pressure and low temperatures is the spinel-type structure (Ross and Navrotsky 1987). The high-temperature phase, olivine-type Mg_2GeO_4 reverts to the spinel-type phase at 1083 K (Dachille and Roy 1960) and persists on quenching to ambient temperature. On compressing the germanate olivine at room-temperatures, it has been reported to stay stable up to 13 GPa, after which new diffraction peaks were observed (Petit et al. 1996) and could not be resolved. Pressure-induced amorphization has been reported above 22-25 GPa (Petit et al. 1996; Nagai et al. 1994). High-pressure Raman spectroscopic studies have observed appearance of new modes at ~11 GPa, followed by a sharp decrease in its intensity at ~25 GPa (Reynard et al. 1994). In this work we aim to resolve the post-olivine structure(s) under compression by studying forsterite-type Mg_2GeO_4 to 105 GPa at both room and high-temperature using laser-heated diamond anvil cells (LH-DAC) and density functional theory (DFT) based computations.

2. Methodology

A. Experimental details

The starting material, olivine-type Mg_2GeO_4 was synthesized by heating high-purity MgO and GeO_2 to 1473 K for 5 days (Ross and Navrotsky 1987; Dutta et al. 2022) and confirmed using Raman spectroscopy and X-ray diffraction. The synthesized sample was ground

3

with 10 wt% gold, which acts as the laser absorber and pressure marker during the high-pressure

experiments. The samples were compressed using symmetric diamond anvil cells with 300 μm –

150 μm diameter culets. Rhenium gaskets were drilled to form the sample chamber. The samples

were loaded inside the sample cavities (200 – 80 μm) and gas loaded with Ne to provide a quasi-

hydrostatic environment. *In situ* X-ray diffraction (XRD) was carried out at sectors 13-ID-D and

16-ID-B of the Advanced Photon Source using a monochromatic beam with wavelengths of

0.2952 Å and 0.4066 Å respectively. The two-dimensional X-ray images were radially integrated

to the one dimensional patterns using DIOPTAS (Prescher and Prakapenka 2015). Double sided

laser heating was used to produce the high temperatures. Temperatures were increased in small

steps of ~100 K and measured using spectroradiometry (Jephcoat and Besedin 1996; Shen et al.

2001). The (111) Au peak was used to calculate the pressures (Fei et al. 2007) using the Birch

Murnaghan equation of state (EOS). The lattice parameters were calculated using least squares

refinement of the peak positions (Holland and Redfern 1997) fitted to Voigt line shapes or whole

profile Le Bail refinement as implemented in the GSAS-II package (Toby and Von Dreele 2013).

The background was fitted with a 6th order Chebyschev polynomial. The unit cell dimensions,

instrumental and sample broadening parameters were initially refined separately and then

together.

B. **Computational details**

All computations were performed using the plane wave implementation of density

functional theory through the Quantum Espresso package (Giannozzi et al. 2009). The

generalized gradient approximation (GGA-PBE, Perdew et al. 1996) was used to treat the

exchange and correlation functional. We have used a plane wave basis set with a cutoff of 40 Ry

and a Monkhorst-Pack (Monkhorst and Pack 1976) *k*-point grid of 6x6x6 for all the considered

structures. Ultrasoft pseudopotentials (Vanderbilt 1990) were used to describe the electron-ion

interactions. The geometry optimizations were carried out using the BFGS algorithm (Broyden

1970) by relaxing the lattice parameters and atomic positions at each pressure step. The

structural relaxations were considered complete when the forces on atoms were less than 1×10^{-4}

Ry/Bohr and total energies were converged to 1×10^{-6} Ry.

3. Results

In three separate experimental runs, the germanate olivine samples were compressed to

peak pressures of 26 GPa, 54 GPa and 105 GPa at room-temperature (Fig. 1). The diffraction

patterns up to 30 GPa can be indexed using the ambient-pressure olivine structure, suggesting a

metastable persistence. As an example, table S1 of the supplementary material shows the

observed and calculated d-spacings for forsterite-type Mg_2GeO_4 at 14.6 GPa. The difference

between the two values is < 0.002 Å, suggesting a good fit of the olivine structure to the

observed pattern. This is also reflected in the whole profile Le Bail refinement of the measured

pattern at 26 GPa (Fig. 2). In contrast to previous studies (Nagai et al. 1994; Petit et al. 1996), we

did not find any evidence for amorphization. The lattice parameters of olivine-type Mg_2GeO_4 at

26 GPa are $a = 4.7573$ Å, $b = 9.6574$ Å and $c = 5.7064$ Å. Figure 3 and table S2 of the

supplementary material shows the change in the unit cell dimensions as a function of pressure.

Although our work extends to higher pressures, it agrees with existing experimental studies,

especially at lower pressures. At higher pressure, the discrepancy possibly arises from the non-

hydrostatic conditions (Klotz et al. 2009) inside the DAC in the previous work. The linear

compressibilities ($\times 10^{-3}$ GPa^{-1}) of the axes for the experimental (theoretical) are $\beta_a = 1.21$ (1.15),

$\beta_b = 2.29$ (2.35), $\beta_c = 1.98$ (1.96). Despite the GGA's tendency to overestimate the lattice

parameters, the remarkable concurrence of experimental and computed linear compressibilities

emphasizes their strong agreement. The order of the axial compressibilities i.e. $\beta_b > \beta_c > \beta_a$ also agree with that of Mg_2SiO_4 forsterite (Zhang 1998; Finkelstein et al. 2014).

Upon further compression to 40 GPa (Fig. 1), new diffraction peaks were observed, which were retained up to the peak pressure of 105 GPa. To understand the structure of the new phase, we computed the enthalpies (Fig. 4) of spinel and post-spinel structures reported in Mg_2SiO_4 and its analogous systems within the germanate framework. The considered structures are: Fo-II, Fo-III, Fo-IV, $CaTi_2O_4$-, $CaFe_2O_4$-, and Ca_2IrO_4-type Mg_2GeO_4 (Decker and Kasper 1957; Babel et al. 1966; Yamanaka et al. 2013; Finkelstein et al. 2014; Bouibes and Zaoui 2020; Dutta et al. 2022); Pv-$MgGeO_3$ (Leinenweber et al. 1994) + B1-MgO and pPv-$MgGeO_3$ (Hirose et al. 2005) + B1-MgO. It can be seen the Pv-$MgGeO_3$ + MgO assemblage becomes more stable (lower enthalpy) with respect to the forsterite- type Mg_2GeO_4 structure at ~12 GPa, which then transforms into the pPv-$MgGeO_3$ +MgO assemblage at ~50 GPa. Taking into account the tendency of the GGA-PBE functional to underestimate transition pressures, these results can be viewed as reasonably consistent with experimental findings (Liu 1977; Hirose et al. 2005). The XRD patterns at P > 40 GPa are not consistent with any of these phases, suggesting the presence of a metastable phase. This can be attributed to the experimental conditions being at room temperature, which creates a kinetic barrier that prevents the transition to the more stable assemblage. Besides Pv-$MgGeO_3$ + MgO and pPv-$MgGeO_3$ + MgO, the candidate phases with low enthalpies are the Fo-II type, Fo-III type and $CaTi_2O_4$-type Mg_2GeO_4 structures. Figure 5 compares the observed XRD pattern at 61 GPa with the simulated diffraction pattern of these three phases. In agreement with a previous theoretical study (Bouibes and Zaoui 2020) on Mg_2SiO_4, the triclinic Fo-II structure (Finkelstein et al. 2014) was neither energetically favored computationally, nor did it match the XRD data. The closest match to the observed patterns were

6

the ordered *Pmma* CaTi$_2$O$_4$-type phase and the Fo-III type phase. Although the simulated

patterns for the two are similar, the Fo-III type structure (CIF on deposit, optimized DFT

structure at 60 GPa) is a better match (fewer peaks) and comparatively lower enthalpy.

Post-spinel (e.g. CaMn$_2$O$_4$-, CaFe$_2$O$_4$- and CaTi$_2$O$_4$- type) structures (Yamanaka et al.

2008) generally feature chains of octahedra that share edges and corners, forming channels that

align parallel to the *c*-axis. The Fo-III structure (Fig. 6) is analogous to an inverse spinel

structure. It is related to the non-centrosymmetric variant of the *Cmcm* CaTi$_2$O$_4$ post-spinel

structure (Yamanaka et al. 2013) in which half of Mg atoms are situated in the larger trigonal

prismatic site (Mg2), while the other half occupy the octahedral (Mg1) site (Finkelstein et al.

2014).This is substantially different from the olivine structure, where both the Mg1 and Mg2

sites are octahedral with one being more distorted than the other. The Fo-III type structure also

marks an increase in the Ge-coordination from 4 (as in olivine) to 6, providing a pathway to the

stable six-coordinated pv and pPv structures. The structural parameters of Fo- and Fo-III type

Mg$_2$GeO$_4$ have been shown in Table 1. Figure 7 shows a Le Bail refinement of the measured

diffraction pattern of Mg$_2$GeO$_4$ at 74 GPa. The difference between the calculated and observed

d-spacings were less than < 0.006 Å (Table S3 of the supplementary material, 68 GPa), again

suggesting a good fit of the measured diffraction patterns with the Fo-III structure. Figure 8 and

table S4 of the supplementary material shows the variation in lattice parameters of Fo-III type

Mg$_2$GeO$_4$ with increasing pressure. The experimental *a*, *b* and *c* parameters are found to decrease

by 2.9%, 2.7% and 2.7% respectively over the pressure range (40.4 GPa – 73.8 GPa) considered.

In agreement with the experiments, the theoretical axial parameters decrease by 3.3%, 3.7% and

3.3% respectively between 40 and 80 GPa. No further transitions were observed up to the peak

pressure of 105 GPa at room-temperature.

The pressure-volume data for both the Fo- and Fo-III type Mg$_2$GeO$_4$ phases (Fig. 9) were fitted to an isothermal 3rd order Birch Murnaghan (BM) equation of state. Table 2 presents the EOS parameters for these phases and includes a comparison with the existing studies on the same structures in Mg$_2$GeO$_4$ (Weidner and Hamaya 1983; Nagai et al. 1994; Petit et al. 1996) and Mg$_2$SiO$_4$ (Andrault et al. 1995; Downs et al. 1996; Zhang 1998; Finkelstein et al. 2014; Zhang et al. 2019; Bouibes and Zaoui 2020). For the germanate olivine, the EOS parameters for the computed data are $V_0 = 316.8$ (3) Å^3, $K_0 = 112.2$ (13) GPa and $K_0' = 3.86$ (5), where V_0, K_0 and K_0' are the unit cell volume, bulk modulus, and its pressure derivative at ambient pressure respectively. In case of the experimentally obtained values, the K_0' was fixed to the theoretical value of 3.86. This yielded $V_0 = 305.1$ (3) and $K_0 = 124.6$ (14) GPa. This is in excellent agreement with existing ultrasonic ($K_0 = 120$ GPa; Soga, 1971) and Brillouin spectroscopic measurements ($K_0 = 120$ GPa; Weidner & Hamaya, 1983). However, the obtained bulk modulus is significantly less than that obtained from previous DAC studies ($K_0 = 166$ (15) at fixed $K_0' = 4$; Petit et al., 1996). The discrepancy likely stems from the limited pressure range (0-10 GPa in the earlier study compared to pressures above 30 GPa in this study). Additionally, the previous work used silicone oil, whereas neon was used in the current study. Silicone oil is known to offer limited hydrostaticity at high pressures (Klotz et al. 2009). The EOS parameters are also in good agreement with the silicate olivine ($K_0 = 130.0$ (9) GPa and $K_0' = 4.12$ (7); Finkelstein et al., 2014). The transition from forsterite- to Fo-III type Mg$_2$GeO$_4$ is expected to have a substantial volume change of 9.53% at 35 GPa, which agrees with its silicate counterpart (8.3% at 58 GPa). In case of Fo-III type Mg$_2$GeO$_4$, the EOS parameters for the theoretical data are: $V_0 = 271.8$ (9) Å^3, $K_0 = 162.9$ (5) GPa and $K_0' = 4.19$ (1). The fit to the experimental data yielded $V_0 = 263.5$ (15) Å^3, $K_0 = 175$ (7) GPa, with K_0' fixed to the computed value (4.19). These values are

8

consistent with the theoretical EOS parameters for Mg_2SiO_4 (V_0 = 247.4517 Å^3, K_0 = 197.12 GPa and K_0' = 3.4; Bouibes and Zaoui 2020).

On laser-heating the Mg_2GeO_4 sample to 2331 ± 148 K for 2-5 minutes at 26 GPa, we observed new diffraction peaks that could not be explained using forsterite-, spinel- or forsterite-III type Mg_2GeO_4 structures. The XRD peaks were instead consistent with an assemblage of Pv-$MgGeO_3$ + B1-MgO. This is in agreement with our computations which predict a transition from the olivine-type structure to Pv-$MgGeO_3$ + MgO at 12 GPa and existing experimental studies with a olivine-type starting material (26 GPa; Liu 1977) as well as a $MgGeO_3$ pyroxene starting material (25 GPa; Runge et al. 2006). The sample was further compressed to 54 GPa at room temperature, followed by heating a fresh spot to a peak temperature of 2463 ± 112 K in small steps of 200 K. The observed diffraction pattern could still be indexed using $MgGeO_3$-Pv + B1-MgO. Figure 10 shows a Le Bail refinement of the XRD pattern at 65 GPa. The lattice obtained from the refinement (a = 4.584 Å, b = 4.858 Å, c = 6.727 Å) are in excellent agreement with previous studies (a = 4.587 Å, b = 4.860 Å, c = 6.721 Å at 65.7 GPa, Runge et al. 2006). In the experiment where a fresh sample was compressed to 105 GPa at room temperature and subsequently heated to 2280 ± 46 K, the diffraction pattern could be explained using a mixture of $CaIrO_3$-type post-perovskite $MgGeO_3$ + B1-MgO (Figure 11). This is consistent with the reported Pv to pPv transition pressure of 63 GPa with a orthoenstatite starting material (Hirose et al. 2005). The lattice parameters obtained from the Le Bail refinement at 110 GPa, 2300 K are (a = 2.567 Å, b = 8.301 Å, c = 6.351 Å) are in agreement with existing experimental work (a = 2.575 Å, b = 8.324 Å, c = 6.349 Å at 107 GPa and 300 K, Kubo et al. 2006).

4. Discussion and Implications

Knowledge of metastable phases are important for understanding the mineralogy of planetary impact sites and meteorites e.g. Martian meteorites NWA 2737 and NWA 1950 (Van de Moortèle et al. 2007). The ultrafast timescales of dynamic compression experiments are often not enough to stabilize the equilibrium stable structures, leading to formation of metastable phases. The metastable olivine wedge hypothesis (Soga 1971; Däßler and Yuen 1996) has commonly been used to explain stagnation of subducting slabs and origin of deep-focus earthquakes. The P, T conditions in the cold subducting slabs may also stabilize metastable phases like Forsterite-III and thereby contribute to the high seismic velocities observed near the 660 km discontinuity (Zhang et al. 2019). The occurrence of the same metastable phases in the germanate analog at significantly lower pressures compared to the silicate (for example, the Fo-III type structure appears at pressures greater than 30 GPa in Mg_2GeO_4 versus 58 GPa in Mg_2SiO_4) enables the use of a broader range of experimental techniques (e.g. Burnley 1990; Burnley et al. 1991). This allows for experiments under more controlled conditions and with larger sample sizes.

Recent laser-based shock compression experiments (Kim et al. 2021) on forsterite Mg_2SiO_4 have shown the presence of a metastable Fo-III phase instead of the stable assemblage i.e. bridgmanite + MgO at pressures > 33 GPa. Mg_2GeO_4 olivine is a widely used analog for forsterite Mg_2SiO_4 and is expected to show similar phase transitions, but at lower pressures. The high-pressure data on the germanate olivine is limited to pressures < 35 GPa and suggest a pressure induced amorphization under compression at room temperature (Nagai et al. 1994; Petit et al. 1996). Using synchrotron X-ray diffraction measurements and density functional computations, we have shown that olivine-type Mg_2GeO_4 persists metastably up to 30 GPa. It

10

then undergoes a pressure induced phase transition to a metastable forsterite-III type structure. The Forsterite-III type phase stays stable up to the peak pressure of 105 GPa (at 300 K), with no evidences of the forsterite-II (Finkelstein et al. 2014) type phase seen in the silicate or pressure induced amorphization. We have also obtained equation of state parameters of both the forsterite- and forsterite-III type phases. Although, our bulk modulus value for forsterite-type Mg_2GeO_4 (K_0 = 124.6 GPa) is lower than previous high-pressure studies (e.g. K_0 = 166 GPa, Petit et al. 1996), it is in excellent agreement with ultrasonic (K_0 = 120 GPa; Soga, 1971) and Brillouin spectroscopic measurements (K_0 = 120 GPa; Weidner & Hamaya, 1983). The enhanced quality of our calculated EOS parameters can be attributed to the utilization of a wider data range and the incorporation of a more hydrostatic pressure medium (Ne). To the best of our knowledge, there is no available data for Fo-III type Mg_2GeO_4.

The Fo-III type phase has now been reported in laser (~10 ns time scale; Kim et al. 2021) and gas gun (~100s of ns; Newman et al. 2018) based shock compression studies as well as static compression experiments in both silicates (Finkelstein et al. 2014) and germanates (this study). This suggests it may be an important transition to pathway to the stable higher-coordination structures at higher temperatures. On laser-heating at 26 and 54 GPa, a partial dissociation into perovskite $MgGeO_3$ + B1-MgO was observed. At 105 GPa, post-perovskite $MgGeO_3$ was observed instead of perovskite. The presence of both the perovskite and post-perovskite structures at high pressures and temperatures in Mg_2GeO_4 makes it an excellent low-pressure analog of Mg_2SiO_4.

5. Acknowledgements

6. References

Andrault, D., Bouhifd, M.A., Itié, J.P., and Richet, P. (1995) Compression and amorphization of $(Mg,Fe)_2SiO_4$ olivines: An X-ray diffraction study up to 70 GPa. Physics and Chemistry of Minerals, 22, 99–107.

Babel, D., Rüdorff, W., and Tschöpp, R. (1966) Ternäre Oxide der Übergangsmetalle. VI. Erdalkaliiridium(IV)-oxide: Struktur von Dicalciumiridium(IV)-oxid, Ca_2IrO_4. Zeitschrift für anorganische und allgemeine Chemie, 347, 282–288.

Bouibes, A., and Zaoui, A. (2020) High-pressure phase transitions of forsterite from first-principles. Journal of Physics and Chemistry of Solids, 136, 109161.

Broyden, C.G. (1970) The convergence of a class of double-rank minimization algorithms 1. General Considerations. IMA Journal of Applied Mathematics, 6, 76–90.

Burnley, P.C. (1990) The effect of nonhydrostatic stress on the olivine-spinel transformation in Mg_2GeO_4. Univ. of Calif., Davis; PhD Thesis.

Burnley, P.C., Green II, H.W., and Prior, D.J. (1991) Faulting associated with the olivine to spinel transformation in Mg_2GeO_4 and its implications for deep-focus earthquakes. Journal of Geophysical Research: Solid Earth, 96, 425–443.

Dachille, F., and Roy, R. (1960) High pressure studies of the system Mg_2GeO_4-Mg_2SiO_4 with special reference to the olivine-spinel transition. American Journal of Science, 258, 225–246.

Däßler, R., and Yuen, D.A. (1996) The metastable olivine wedge in fast subducting slabs: Constraints from thermo-kinetic coupling. Earth and Planetary Science Letters, 137, 109–118.

Decker, B.F., and Kasper, J.S. (1957) The structure of calcium ferrite. Acta Crystallographica, 10, 332–337.

Downs, R.T., Zha, C.S., Duffy, T.S., and Finger, L.W. (1996) The equation of state of forsterite to 17.2 GPa and effects of pressure media. American Mineralogist, 81, 51–55.

Dutta, R., Tracy, S.J., Stan, C.V., Prakapenka, V.B., Cava, R.J., and Duffy, T.S. (2018) Phase stability of iron germanate, $FeGeO_3$, to 127 GPa. Physics and Chemistry of Minerals, 45, 367–379.

Dutta, R., Greenberg, E., Prakapenka, V.B., and Duffy, T.S. (2019) Phase transitions beyond post-perovskite in $NaMgF_3$ to 160 GPa. Proceedings of the National Academy of Sciences, 116, 19324–19329.

Dutta, R., Tracy, S.J., Cohen, R.E., Miozzi, F., Luo, K., Yang, J., Burnley, P.C., Smith, D., Meng, Y., Chariton, S., and others (2022) Ultrahigh-pressure disordered eight-coordinated phase of Mg_2GeO_4: Analogue for super-Earth mantles. Proceedings of the National Academy of Sciences, 119, e2114424119.

Dutta, R., Tracy, S.J., and Cohen, R.E. (2023) High-pressure order-disorder transition in Mg_2SiO_4: Implications for super-Earth mineralogy. Physical Review B, 107, 184112.

Fei, Y., Ricolleau, A., Frank, M., Mibe, K., Shen, G., and Prakapenka, V. (2007) Toward an internally consistent pressure scale. Proceedings of the National Academy of Sciences, 104, 9182–9186.

Finkelstein, G.J., Dera, P.K., Jahn, S., Oganov, A.R., Holl, C.M., Meng, Y., and Duffy, T.S. (2014) Phase transitions and equation of state of forsterite to 90 GPa from single-crystal X-ray diffraction and molecular modeling. American Mineralogist, 99, 35–43.

Giannozzi, P., Baroni, S., Bonini, N., Calandra, M., Car, R., Cavazzoni, C., Ceresoli, D., Chiarotti, G.L., Cococcioni, M., Dabo, I., and others (2009) QUANTUM ESPRESSO: a modular and open-source software project for quantum simulations of materials. Journal of Physics: Condensed Matter, 21, 395502.

Grocholski, B., Shim, S.-H., and Prakapenka, V.B. (2010) Stability of the $MgSiO_3$ analog $NaMgF_3$ and its implication for mantle structure in super-Earths. Geophysical Research Letters, 37, L14204.

Guyot, F., and Reynard, B. (1992) Pressure-induced structural modifications and amorphization in olivine compounds. Chemical Geology, 96, 411–420.

Hirose, K., Kawamura, K., Ohishi, Y., Tateno, S., and Sata, N. (2005) Stability and equation of state of $MgGeO_3$ post-perovskite phase. American Mineralogist, 90, 262–265.

Holland, T.J.B., and Redfern, S.A.T. (1997) Unit cell refinement from powder diffraction data; the use of regression diagnostics. Mineralogical Magazine, 61, 65–77.

Jephcoat, A.P., and Besedin, S.P. (1996) Temperature measurement and melting determination in the laser-heated diamond-anvil cell. Philosophical Transactions: Mathematical, Physical and Engineering Sciences, 354, 1333–1360.

Kim, D., Tracy, S.J., Smith, R.F., Gleason, A.E., Bolme, C.A., Prakapenka, V.B., Appel, K., Speziale, S., Wicks, J.K., Berryman, E.J., and others (2021) Femtosecond X-Ray Diffraction of Laser-Shocked Forsterite (Mg2SiO4) to 122 GPa. Journal of Geophysical Research: Solid Earth, 126, e2020JB020337

Klotz, S., Chervin, J.-C., Munsch, P., and Marchand, G.L. (2009) Hydrostatic limits of 11 pressure transmitting media. Journal of Physics D: Applied Physics, 42, 075413.

Kubo, A., Kiefer, B., Shen, G., Prakapenka, V.B., Cava, R.J., and Duffy, T.S. (2006) Stability and equation of state of the post-perovskite phase in $MgGeO_3$ to 2 Mbar. Geophysical Research Letters, 33, L12S12.

Leinenweber, K., Wang, Y., Yagi, T., and Yusa, H. (1994) An unquenchable perovskite phase of $MgGeO_3$ and comparison with $MgSiO_3$ perovskite. American Mineralogist, 79, 197–199.

Liu, L. (1977) The post-spinel phases of twelve silicates and germanates in M.H. Manghnani and S.-I. Akimoto, Eds., High-Pressure Research pp. 245–253. Academic Press.

Monkhorst, H.J., and Pack, J.D. (1976) Special points for Brillouin-zone integrations. Physical Review B, 13, 5188–5192.

Murakami, M., Hirose, K., Kawamura, K., Sata, N., and Ohishi, Y. (2004) Post-perovskite phase transition in $MgSiO_3$. Science, 304, 855–858.

Nagai, T., Yano, K., Dejima, M., and Yamanaka, T. (1994) Pressure-induced amorphization of Mg_2GeO_4-olivine. Mineralogical Journal, 17, 151–157.

Newman, M.G., Kraus, R.G., Akin, M.C., Bernier, J.V., Dillman, A.M., Homel, M.A., Lee, S., Lind, J., Mosenfelder, J.L., Pagan, D.C., and others (2018) In situ observations of phase changes in shock compressed forsterite. Geophysical Research Letters, 45, 8129–8135.

Oganov, A.R., and Ono, S. (2004) Theoretical and experimental evidence for a post-perovskite phase of $MgSiO_3$ in Earth's D" layer. Nature, 430, 445–448.

Perdew, J.P., Burke, K., and Ernzerhof, M. (1996) Generalized Gradient Approximation made simple. Physical Review Letters, 77, 3865–3868.

Petit, P.E., Guyot, F., Fiquet, G., and Itié, J.P. (1996) High-pressure behaviour of germanate olivines studied by X-ray diffraction and X-ray absorption spectroscopy. Physics and Chemistry of Minerals, 23, 173–185.

Prescher, C., and Prakapenka, V.B. (2015) DIOPTAS: a program for reduction of two-dimensional X-ray diffraction data and data exploration. High Pressure Research, 35, 223–230.

Reynard, B., Petit, P.-E., Guyot, F., and Gillet, P. (1994) Pressure-induced structural modifications in Mg_2GeO_4-olivine: A Raman spectroscopic study. Physics and Chemistry of Minerals, 20, 556–562.

Ringwood, A.E. (1991) Phase transformations and their bearing on the constitution and dynamics of the mantle. Geochimica et Cosmochimica Acta, 55, 2083–2110.

Ringwood, A.E., and Seabrook, M. (1963) High-pressure phase transformations in germanate pyroxenes and related compounds. Journal of Geophysical Research, 68, 4601–4609.

Ross, N.L., and Navrotsky, A. (1987) The Mg_2GeO_4 olivine-spinel phase transition. Physics and Chemistry of Minerals, 14, 473–481.

Rouquette, J., Kantor, I., McCammon, C.A., Dmitriev, V., and Dubrovinsky, L.S. (2008) High-pressure studies of $(Mg_{0.9}Fe_{0.1})_2SiO_4$ olivine using Raman spectroscopy, X-ray diffraction, and Mössbauer spectroscopy. Inorganic Chemistry, 47, 2668–2673.

Runge, C.E., Kubo, A., Kiefer, B., Meng, Y., Prakapenka, V.B., Shen, G., Cava, R.J., and Duffy, T.S. (2006) Equation of state of $MgGeO_3$ perovskite to 65 GPa: comparison with the post-perovskite phase. Physics and Chemistry of Minerals, 33, 699–709.

Shen, G., Rivers, M.L., Wang, Y., and Sutton, S.R. (2001) Laser heated diamond cell system at the Advanced Photon Source for in situ x-ray measurements at high pressure and temperature. Review of Scientific Instruments, 72, 1273–1282.

Soga, N. (1971) Sound velocity of some germanate compounds and its relation to the law of corresponding states. Journal of Geophysical Research (1896-1977), 76, 3983–3989.

Toby, B.H., and Von Dreele, R.B. (2013) GSAS-II: the genesis of a modern open-source all purpose crystallography software package. Journal of Applied Crystallography, 46, 544–549.

Tsuchiya, T., Tsuchiya, J., Umemoto, K., and Wentzcovitch, R.M. (2004) Phase transition in $MgSiO_3$ perovskite in the Earth's lower mantle. Earth and Planetary Science Letters, 224, 241–248.

Umemoto, K., and Wentzcovitch, R.M. (2019) Ab initio exploration of post-PPV transitions in low-pressure analogs of $MgSiO_3$. Physical Review Materials, 3, 123601.

Umemoto, K., and Wentzcovitch, R.M. (2021) Ab initio prediction of an order-disorder transition in Mg_2GeO_4: Implication for the nature of super-Earth's mantles. Physical Review Materials, 5, 093604.

Umemoto, K., Wentzcovitch, R.M., Wu, S., Ji, M., Wang, C.-Z., and Ho, K.-M. (2017) Phase transitions in MgSiO3 post-perovskite in super-Earth mantles. Earth and Planetary Science Letters, 478, 40–45.

van de Moortèle, B., Reynard, B., McMillan, P.F., Wilson, M., Beck, P., Gillet, P., and Jahn, S. (2007) Shock-induced transformation of olivine to a new metastable $(Mg,Fe)_2SiO_4$ polymorph in Martian meteorites. Earth and Planetary Science Letters, 261, 469–475.

van den Berg, A.P., Yuen, D.A., Umemoto, K., Jacobs, M.H.G., and Wentzcovitch, R.M. (2019) Mass-dependent dynamics of terrestrial exoplanets using ab initio mineral properties. Icarus, 317, 412–426.

Vanderbilt, D. (1990) Soft self-consistent pseudopotentials in a generalized eigenvalue formalism. Physical Review B, 41, 7892–7895.

Weidner, D.J., and Hamaya, N. (1983) Elastic properties of the olivine and spinel polymorphs of Mg_2GeO_4, and evaluation of elastic analogues. Physics of the Earth and Planetary Interiors, 33, 275–283.

Yamanaka, T., Uchida, A., and Nakamoto, Y. (2008) Structural transition of post-spinel phases $CaMn_2O_4$, $CaFe_2O_4$, and $CaTi_2O_4$ under high pressures up to 80 GPa. American Mineralogist, 93, 1874–1881.

Yamanaka, T., Kyono, A., Nakamoto, Y., Meng, Y., Kharlamova, S., Struzhkin, V.V., and Mao, H. (2013) High-pressure phase transitions of $Fe_{3-x}Ti_xO_4$ solid solution up to 60 GPa correlated with electronic spin transition. American Mineralogist, 98, 736–744.

Zhang, L. (1998) Single crystal hydrostatic compression of $(Mg,Mn,Fe,Co)_2SiO_4$ olivines. Physics and Chemistry of Minerals, 25, 308–312.

Zhang, Y., Zhang, Y., Liu, Y., and Liu, X. (2019) A metastable Fo-III wedge in cold slabs subducted to the lower part of the mantle transition zone: A hypothesis based on first-principles simulations. Minerals, 9, 186.

Figure Captions

Figure 1. Selected X-ray diffraction patterns ($\lambda = 0.4066$) of Mg_2GeO_4 under compression at room-temperature. Au, Ne, Re, Fo and Fo-III indicate the peaks from gold, neon, rhenium, forsterite-, and forsterite-III type Mg_2GeO_4, respectively.

Figure 2. Le Bail refinement of the X-ray diffraction pattern ($\lambda = 0.4066$) of Mg_2GeO_4 at 26 GPa and 300 K. Black crosses show the observed spectrum. Red, green, and blue lines indicate the calculated spectrum, background, and difference between observed and fitted spectra respectively. The colored bars at the bottom show the different phases.

Figure 3. Change in lattice parameters of forsterite-type Mg_2GeO_4 with pressure. The solid data points represent this study (red: experiments, blue: DFT-PBE), while the open symbols show existing experimental studies (yellow: Petit et al. 1996), purple: Nagai et al. 1994). The lattice parameters of Mg_2SiO_4 (Finkelstein et al. 2014) have also been shown for comparison (open green symbols).

Figure 4. Enthalpy difference of the different phases of Mg_2GeO_4 with respect to the Forsterite-III type phase at 0 K.

Figure 5. Comparison of the observed XRD pattern ($\lambda = 0.4066$) at 61 GPa with the simulated patterns of the computed Fo-II, Fo-III and *Pmma* $CaTi_2O_4$-type Mg_2GeO_4 structures at 60 GPa.

Figure 6. Crystal structure of forsterite- and forsterite-III type Mg_2GeO_4. Mg1 and Mg2 indicate the two inequivalent magnesium sites.

Figure 7. Le Bail refinement of XRD pattern ($\lambda = 0.4066$) of Mg_2GeO_4 at 74 GPa and 300 K. Colors have the same meaning as figure 2.
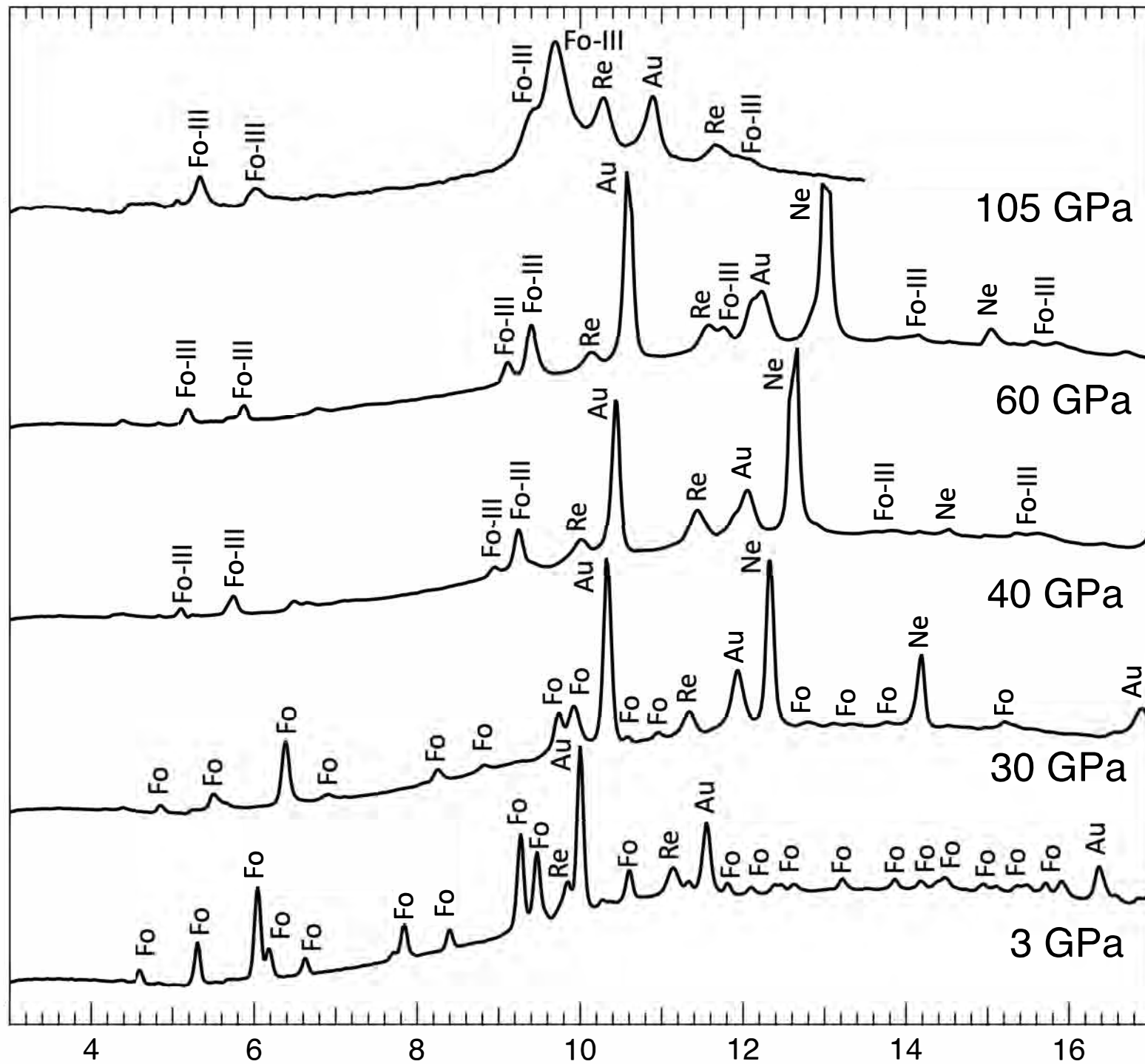
Figure 8. Lattice parameters of Fo-III type Mg_2GeO_4 versus pressure. Solid orange and blue indicate our experimental and theoretical data respectively. Open green symbols show the Mg_2SiO_4 data (Finkelstein et al. 2014).

Figure 9. Variation in unit cell volume as a function of pressure. Red and orange solid circles represent the experimental data for Fo- and Fo-III type Mg_2GeO_4, respectively, while dark and light blue indicate the corresponding theoretical data for these two phases. Solid lines are 3rd order BM fits to the data. Yellow (Petit et al. 1996) and purple (Nagai et al. 1994) open symbols show existing experimental data on forsterite-type Mg_2GeO_4. Open green symbols in dark and light green represent the silicate data for the same phases, respectively (Finkelstein et al. 2014).

Figure 10. Le Bail refinement of the X-ray diffraction pattern ($\lambda = 0.4066$) of Mg_2GeO_4 after laser heating to 2460 K and then quenching to room temperature at 65 GPa. The colored bars indicate the different phases.
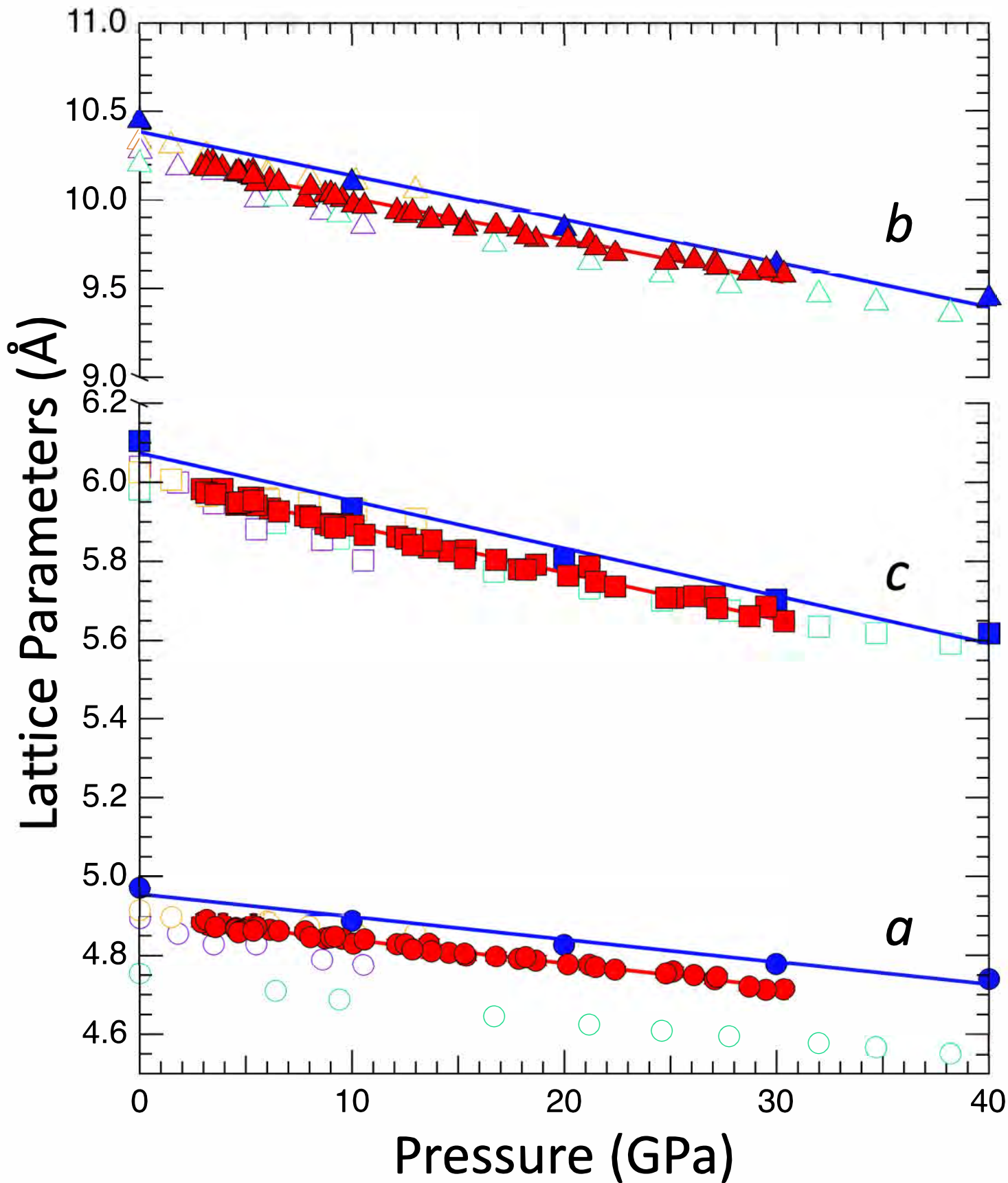
Figure 11. Le Bail refinement of the diffraction pattern ($\lambda = 0.4066$) of Mg_2GeO_4 at 110 GPa and 2280 K. The different phases are represented by colored sticks at the bottom.

Fo-III

Au

Ne
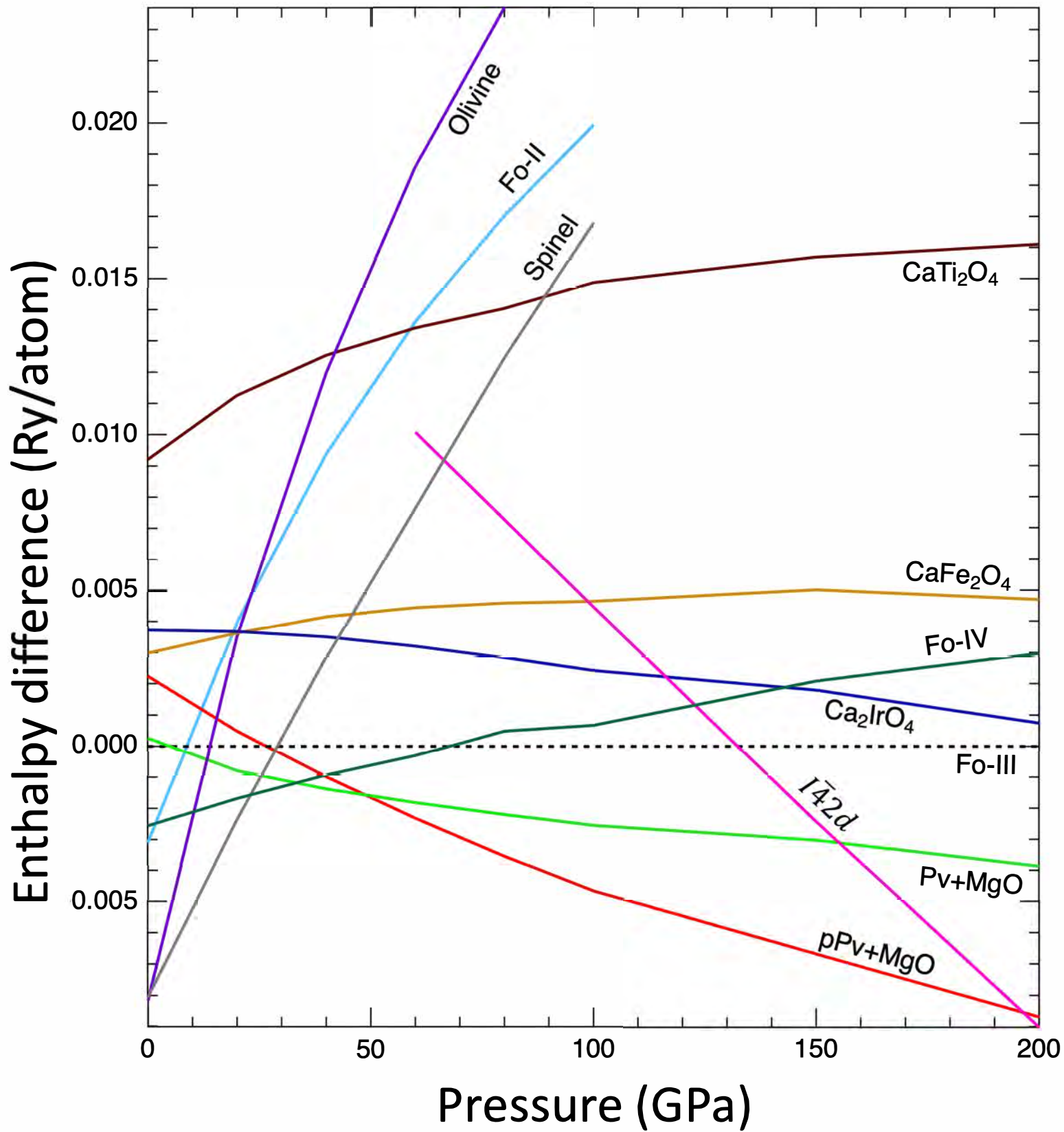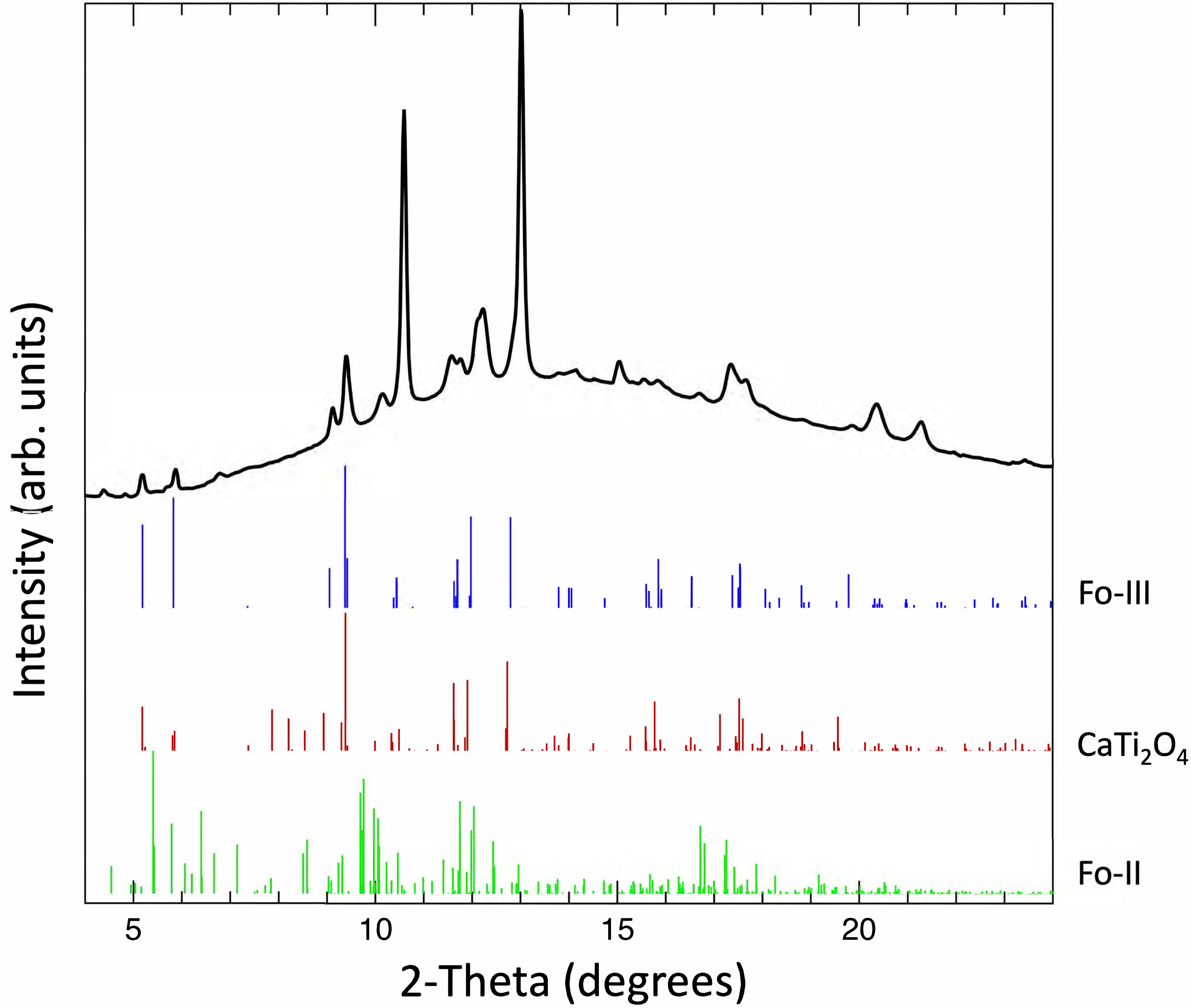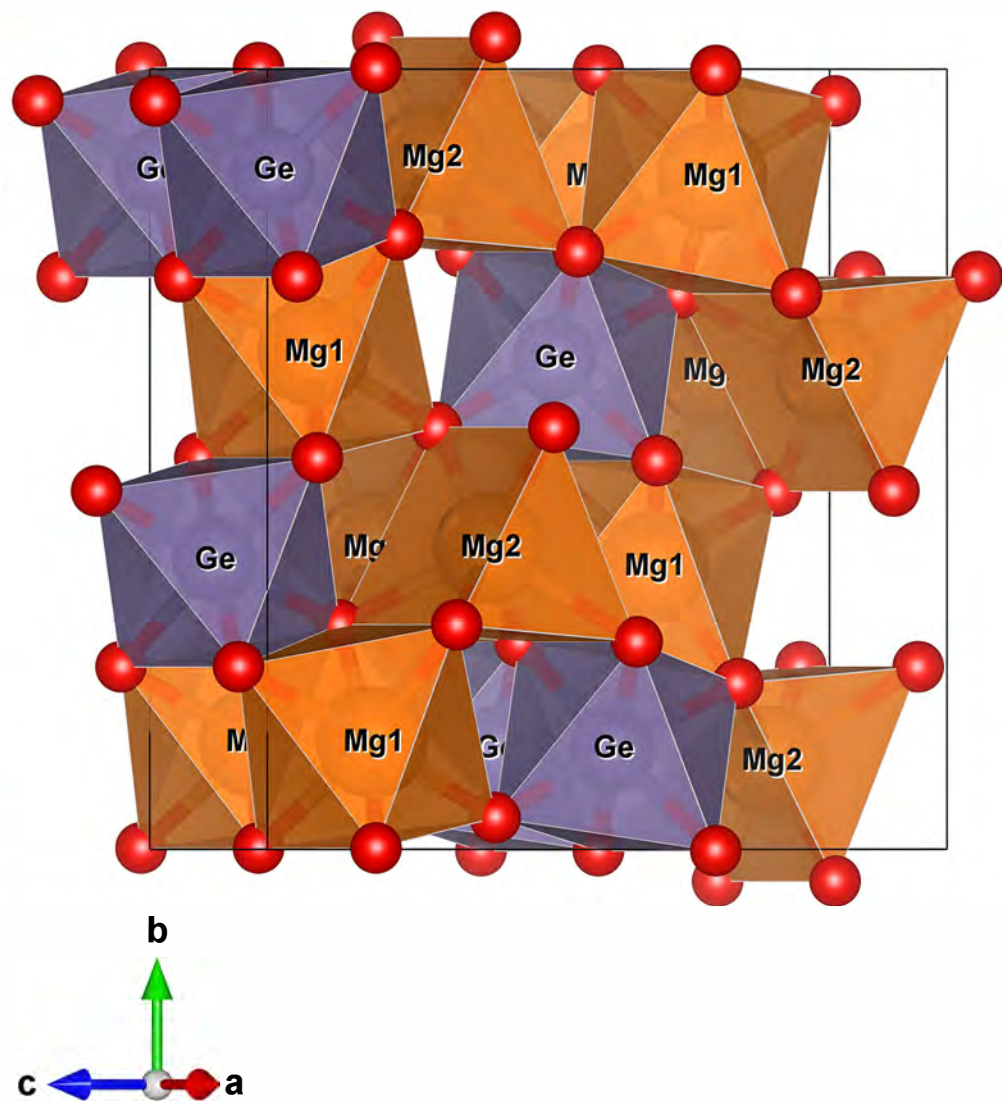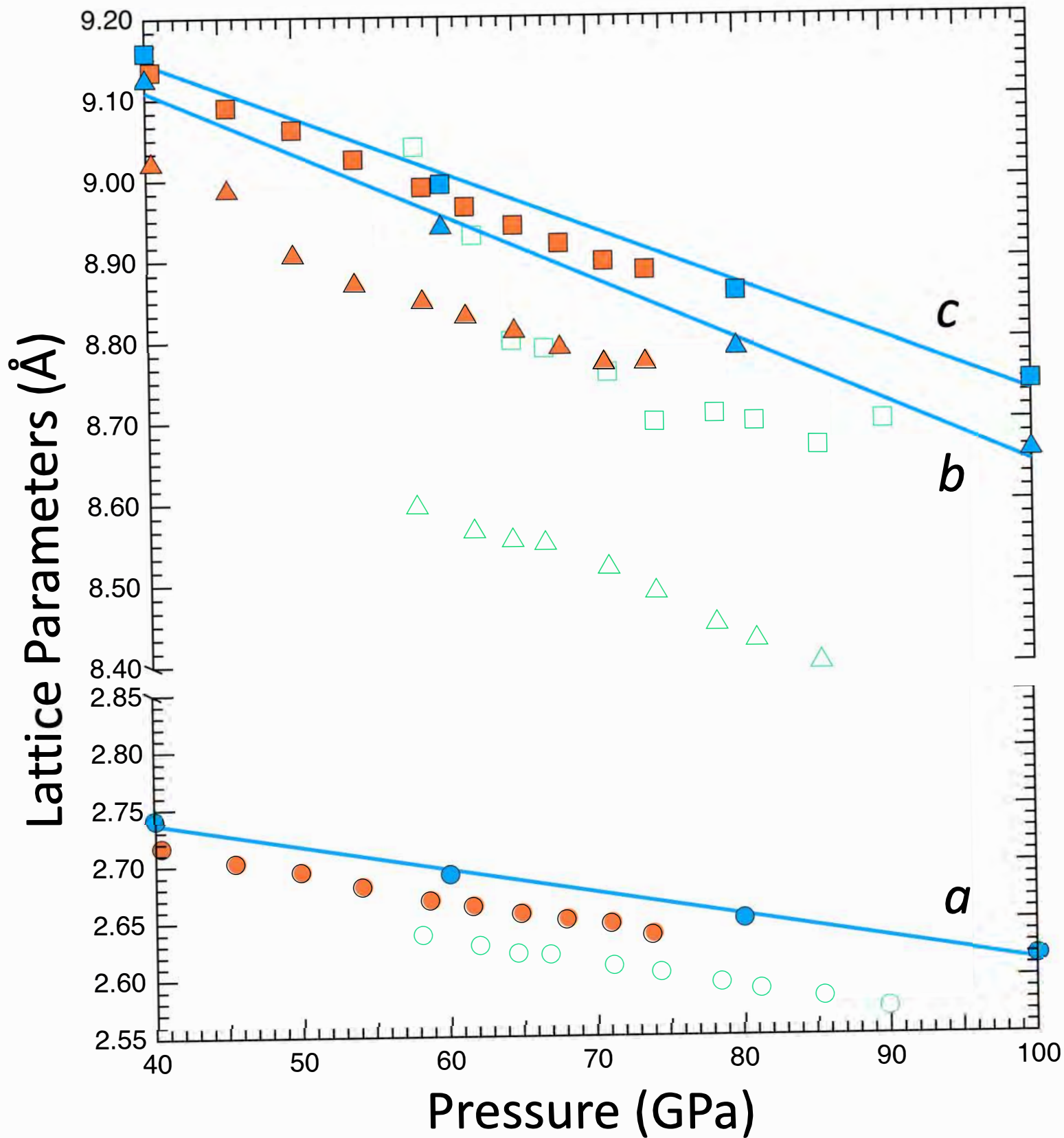
Re
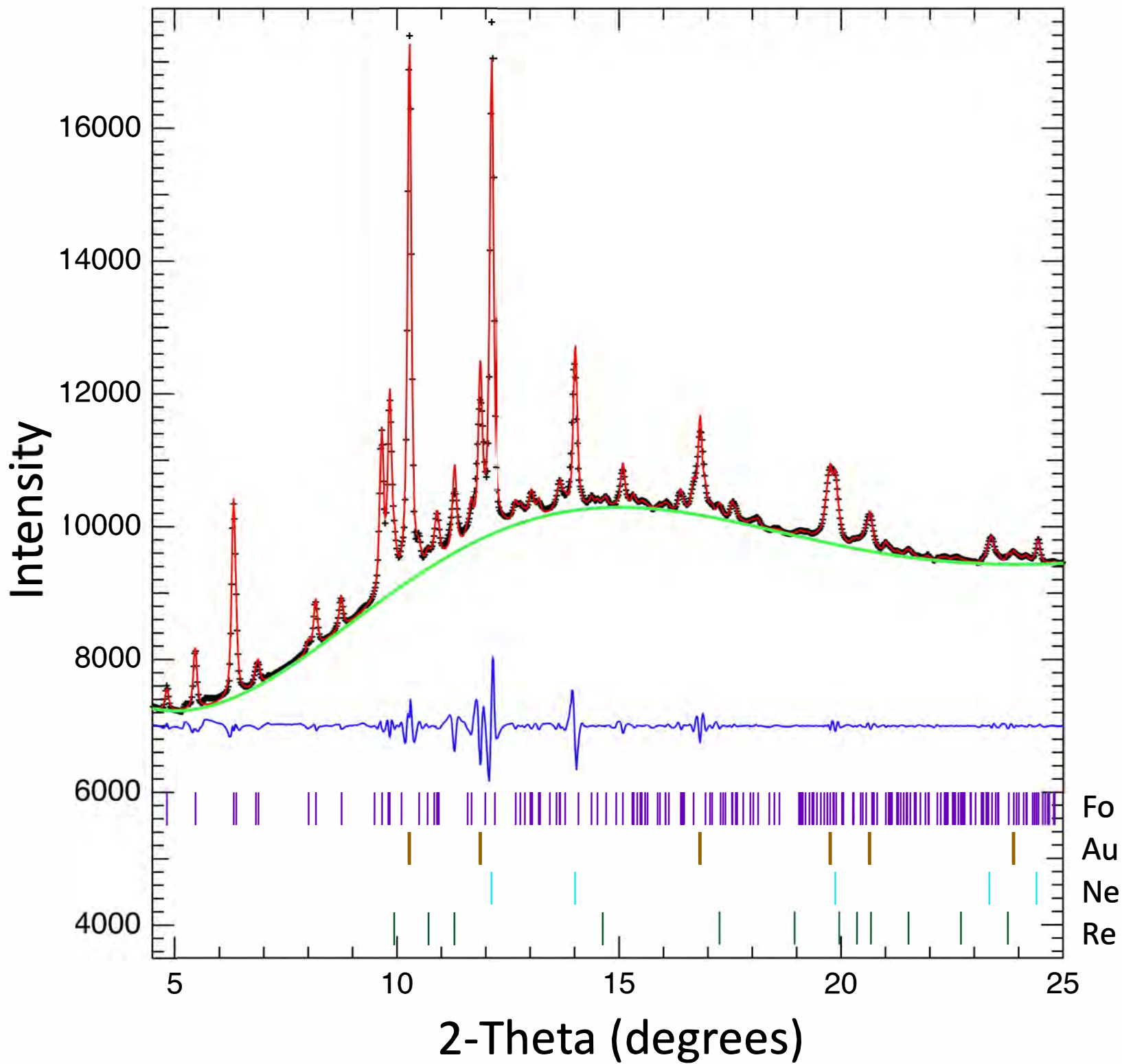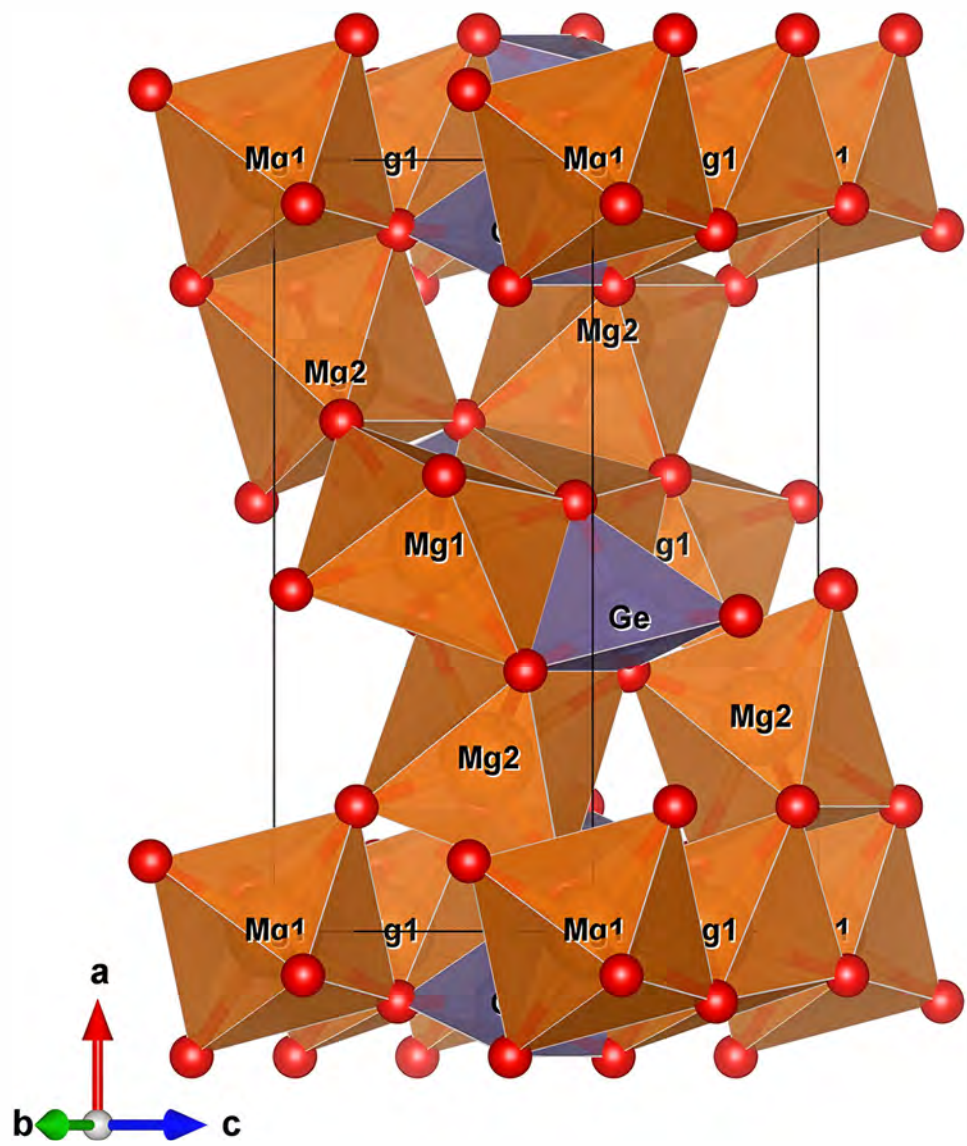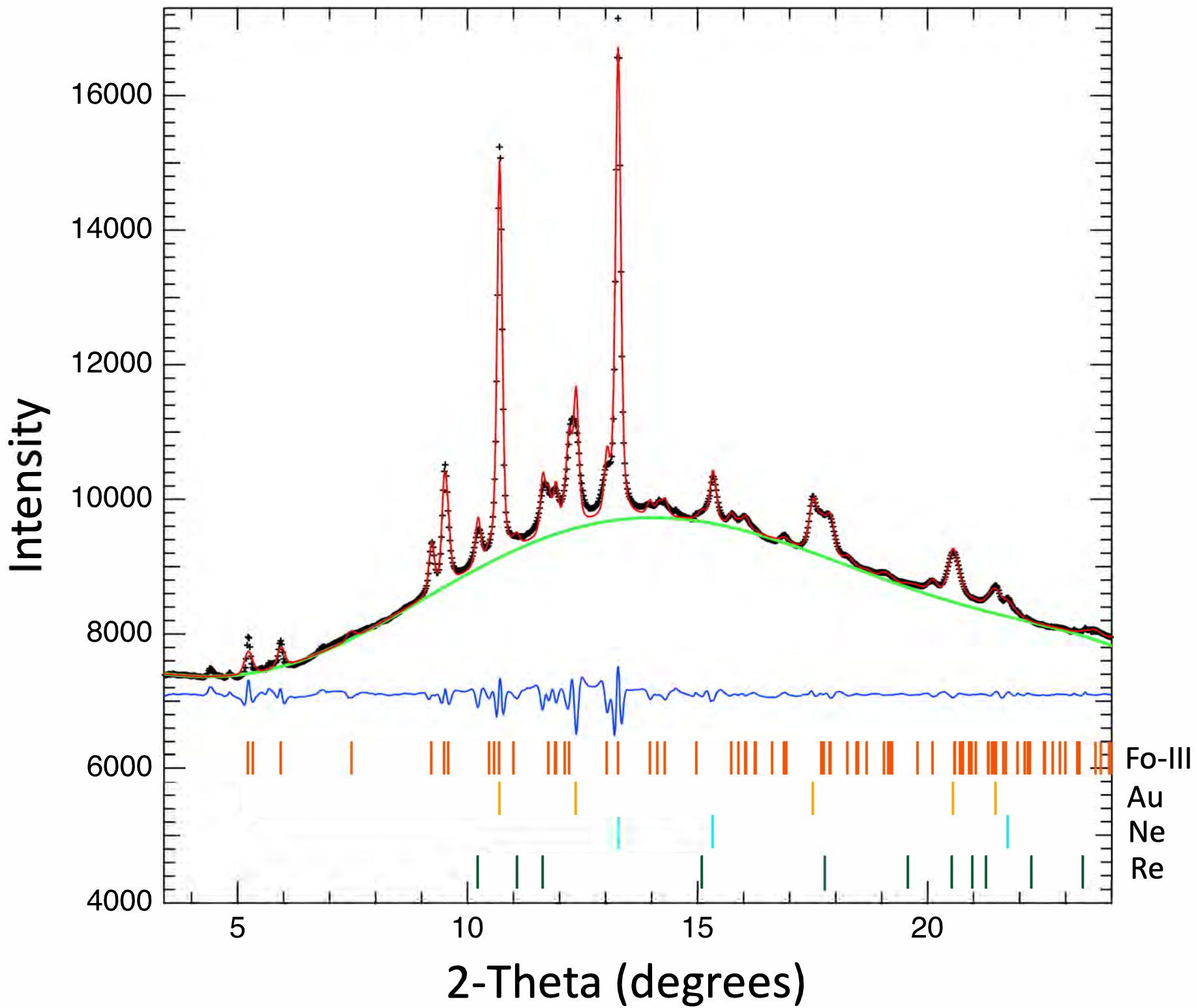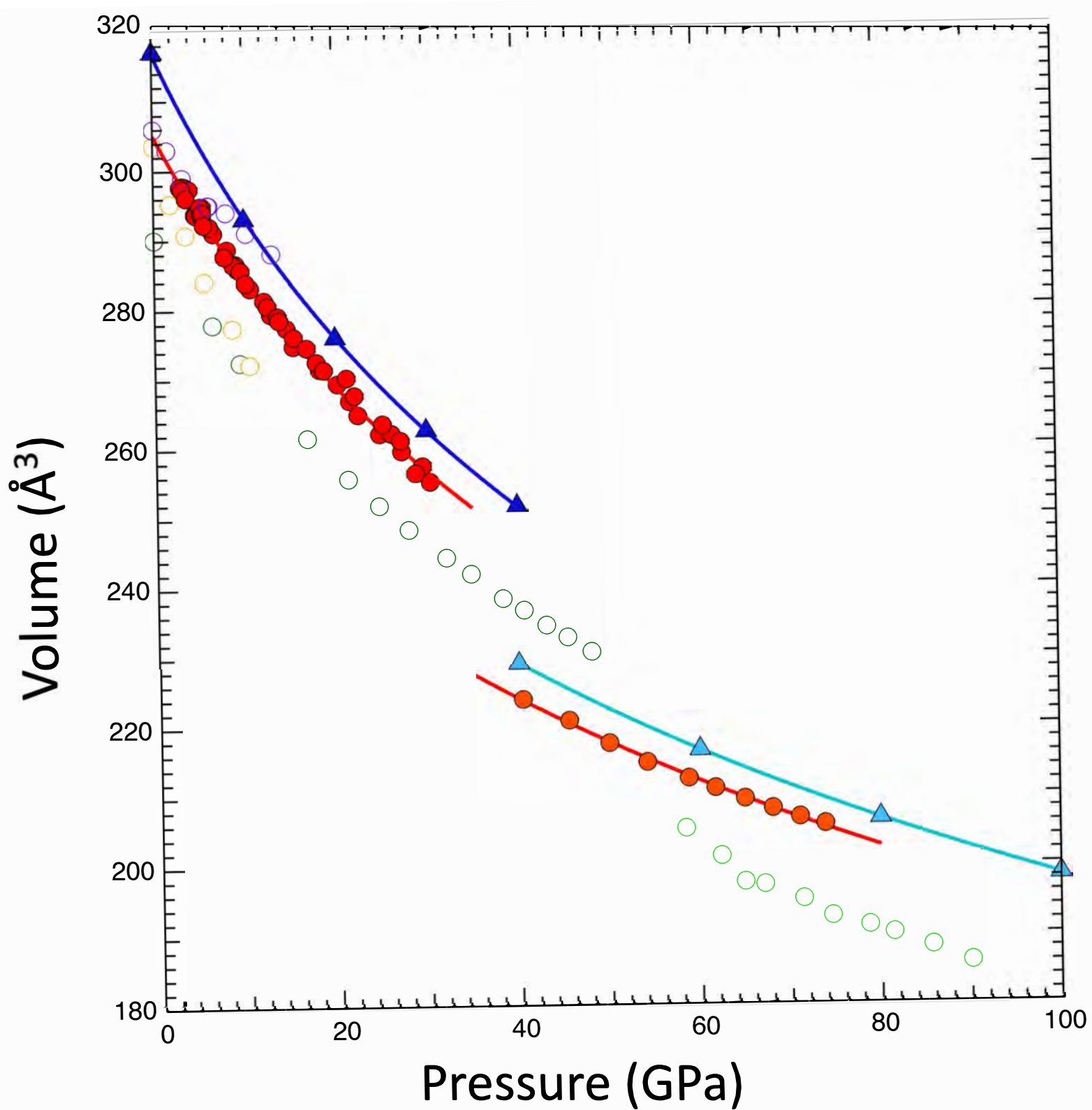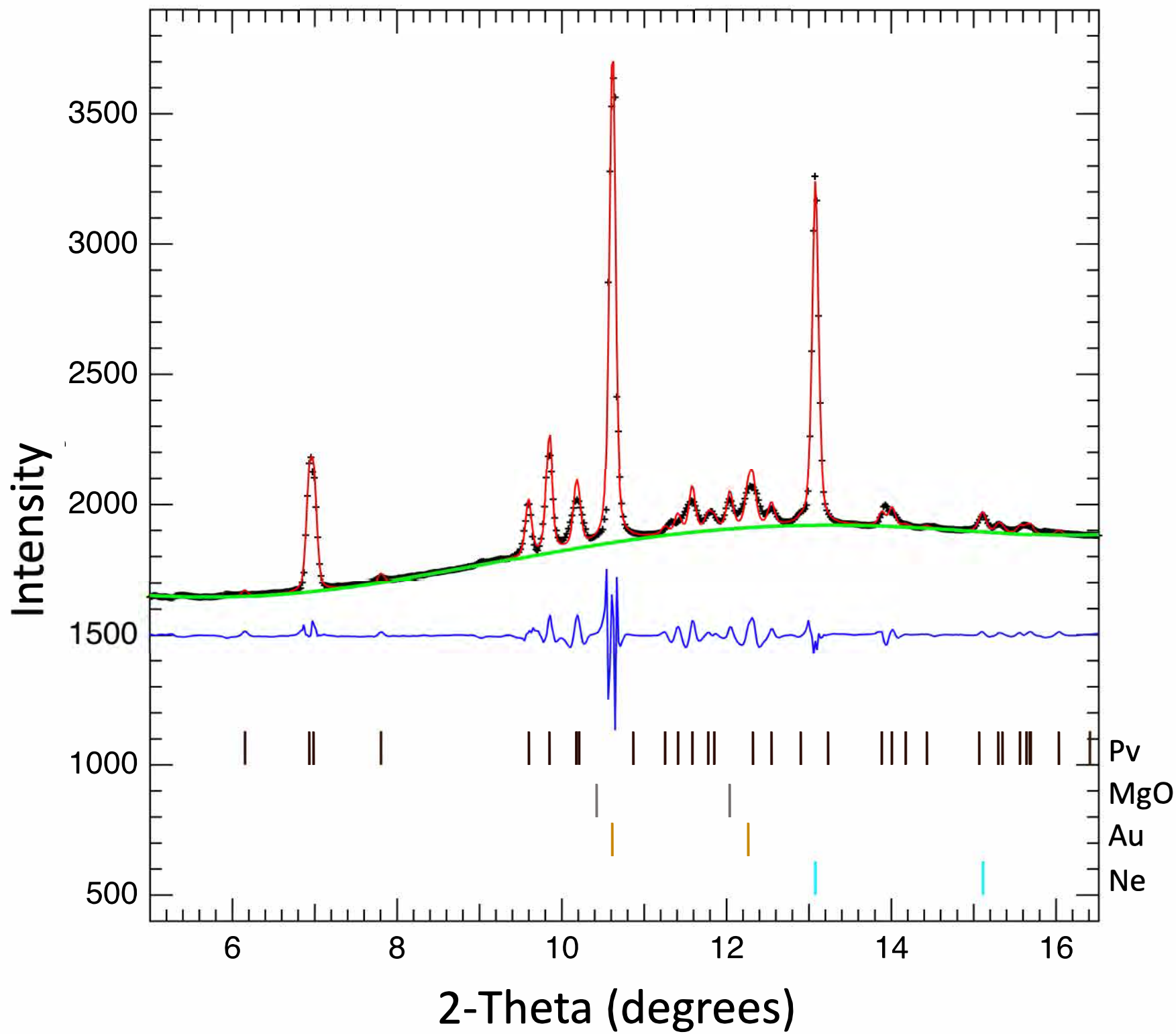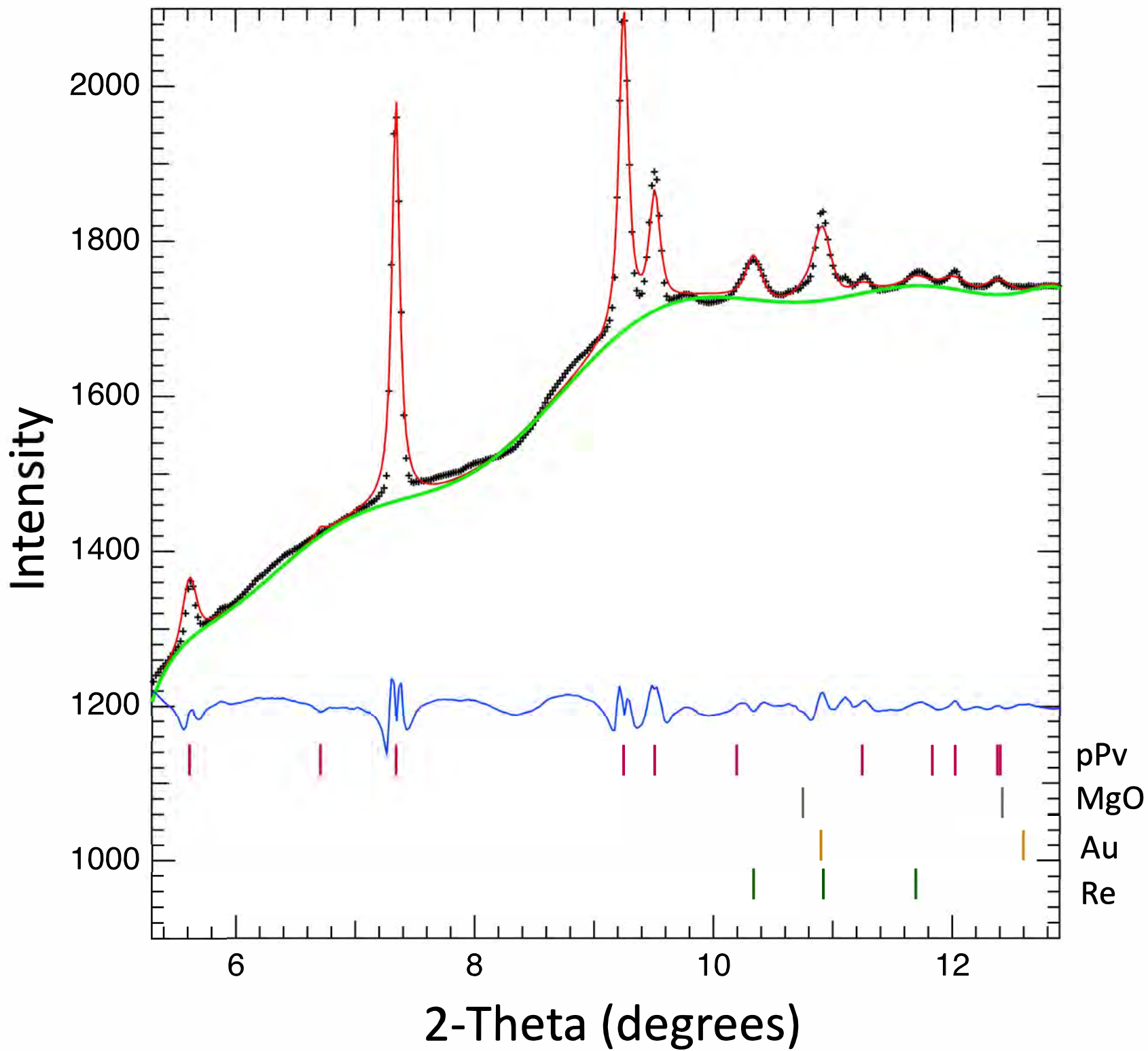
Table 1. Structural parameters of forsterite- and forsterite-III type Mg_2GeO_4.

Phase		Lattice Parameters			Atomic Positions			
		a (Å)	b (Å)	c (Å)	Atom	x	y	z
Forsterite-type	DFT (0 GPa)	10.445	6.104	4.971	Mg1	0	0	0
					Mg2	0.77617	0.25	0.49341
					Ge	0.59424	0.25	-0.06409
					O1	0.59210	0.25	0.28914
					O2	-0.05998	0.25	0.73013
					O3	0.66431	0.02121	0.76671
	Exp (2.9 GPa)	4.884 (7)	10.188 (7)	5.983 (4)				
Fo-III type	DFT (60 GPa)	2.692	8.940	8.994	Mg1	0	0.86261	0.34586
					Mg2	0	0.38687	0.67328
					Ge	0	0.87087	-0.00852
					O1	0	0.49826	0.42649
					O2	0	0.76602	0.54234
					O3	0	0.21248	0.30784
					O4	0	-0.04071	0.16471
	Exp (61.6 GPa)	2.664 (1)	8.831 (7)	8.966 (6)				

Table 2. Equation of state parameters for forsterite- and forsterite-III type Mg_2GeO_4 and Mg_2SiO_4.

Phase	Mg_2GeO_4				Mg_2SiO_4			
	V_0 (Å^3)	K_0 (GPa)	K_0'	Reference	V_0 (Å^3)	K_0 (GPa)	K_0'	Reference
Forsterite - type	316.8 (3)	112.2 (13)	3.86 (5)	This study (DFT)	290.1 (1)	130.0 (9)	4.12 (7)	Finkelstein et al., 2014 (Exp)
	305.1 (3)	124.6 (14)	3.86 (fixed)	This study (Exp)	289.17	128 (8)	4 (fixed)	Andrault et al., 1995 (Exp)
	303	70 (5)	-	Nagai et al., 1994 (Exp)	289.3 (1)	128.8 (5)	4.2 (2)	Zhang., 1998 (Exp)
	306 (4)	166 (15)	4 (fixed)	Petit et al., 1996 (Exp)				
	305.4	120	-	Weidner and Hamaya., 1984 (Exp)	290.14 (9)	125 (2)	4.0 (4)	Downs et al., 1996 (Exp)
Forsterite -III type	271.8 (9)	162.9 (5)	4.19 (1)	This study (DFT)	247.4	197	3.4	Bouibes and Zaoui., 2020 (DFT)
	263.5 (15)	175 (7)	4.19 (fixed)	This study (Exp)	249.17	184.9 (8)	4.11 (5)	Zhang et al., 2019 (DFT)